3

Slow Sound and Critical Coupling to Design Deep Subwavelength Acoustic Metamaterials for Perfect Absorption and Efficient Diffusion

The control of both the absorption and the diffusion of sound constitutes two prominent research lines in audible acoustics. The acoustic absorbers and diffusers developed up to now are efficient in the high frequency range with sizes comparable to the wavelength of the working frequency. On the contrary, in the low frequency regime, huge dimensions leading to oversized treatments and high manufacture costs arise. In this chapter, we discuss acoustic metamaterials showing efficient absorption and diffusion at low frequencies with a deep subwavelength size. On the one hand, by exploiting the slow sound effect, the resonance frequencies of the system can be shifted down to the low frequency range and the phase shift of the reflection coefficient can be perfectly tuned. On the other hand, the critical coupling conditions are introduced to achieve a perfect impedance matching allowing perfect absorption conditions. We will show in detail both an ultra-thin absorber and ultra-thin diffusers working in the low frequency regime.

3.1. Introduction

Acoustics metamaterials have recently revolutionized the field of acoustics and mechanics due to their extraordinary functionalities giving rise to breakthroughs in the material design strategy. Common wall treatments are made of flat panels with poor efficiency at low frequencies to attenuate, absorb or diffuse acoustic waves.

Chapter written by Vicente ROMERO-GARCÍA, Noé JIMÉNEZ and Jean-Philippe GROBY.

Fundamentals and Applications of Acoustic Metamaterials: From Seismic to Radio Frequency,
First Edition. Edited by Vicente Romero-García and Anne-Christine Hladky-Hennion.
© ISTE Ltd 2019. Published by ISTE Ltd and John Wiley & Sons, Inc.

In order to be efficient at low frequencies, we have to solve a complex problem: reducing the geometric dimensions of the structure while increasing the density of states at low frequencies and finding the good conditions to match or tune the acoustic impedance.

Acoustic metamaterials have been proposed as a successful approach for increasing the density of states at low frequencies with reduced dimensions. Recently, several possibilities based on these systems have been used to design sound absorbing structures or efficient diffusers which can simultaneously present subwavelength dimensions and very good efficiency. On the one hand, the design of subwavelength structures can be achieved by using different strategies. One of them consists of using space-coiling structures [CAI 14, LI 16]. Another way is to use subwavelength resonators as membranes [YAN 08, MEI 12] or Helmholtz resonators (HRs) [MER 15, ACH 16]. Recently, a new type of subwavelength metamaterial based on the concept of slow sound propagation has been used for the same purpose [GRO 15, GRO 16]. This last type of metamaterial makes use of its strong dispersion for generating slow sound conditions inside the material [THE 14] and, therefore, drastically decreasing working frequency. Hence, the structure thickness becomes deeply subwavelength. On the other hand, the impedance matching of such open, lossy and resonant structures can be achieved by the well-known critical coupling condition [ROM 16b, JIM 17b, JIM 18, BLI 08]. These open systems, at the resonant frequency, are characterized by both the leakage rate of energy (i.e. the coupling of the resonant elements with the propagating medium) and the intrinsic losses of the resonator. The balance between the leakage and the losses activates the condition of critical coupling, trapping the energy around the resonant elements and generating a maximum of energy absorption. In the case of transmission systems, degenerate critically coupled resonators with symmetric and antisymmetric resonances should be used to perfectly absorb the incoming energy by trapping the energy in the resonant element, i.e. without reflection or transmission [PIP 14, YAN 15]. In the case of a purely reflecting system, either symmetric or antisymmetric resonances that are critically coupled can be used to obtain perfect absorption of energy by a perfect trapping of energy around the resonators [MA 14, ROM 16a].

In this chapter, we discuss two types of acoustic metamaterial, both based on slow sound and critical coupling conditions, showing efficient absorption [JIM 16a, JIM 17d, JIM 17c] and diffusion [JIM 17a] at low frequencies with a deep subwavelength size. In both cases, the system will consist of a 2D flat panel composed of a periodic distribution of slits loaded by a finite array of HR. By exploiting the slow sound effect, the resonance frequencies of the system can be shifted down to the low frequency range and the phase shift of the reflection coefficient can be perfectly tuned. On the contrary, the critical coupling conditions are introduced to achieve a perfect impedance matching allowing perfect absorption conditions. We will show in detail both an ultra-thin absorber and ultra-thin diffusers both working in the low frequency regime.

3.2. Building block of the acoustic metamaterial: finite slit loaded with Helmholtz resonators

We consider a 2D flat panel composed of a periodic distribution of slits of width h separated a distance d and distributed in the x_1 direction as shown in Figure 3.1(a). Each slit is loaded by a finite array of M Helmholtz resonators (HRs) separated with lattice constant (distance between HRs) a. The HRs considered in this work can be either 2D (Figure 3.1(b)), made of a combination of slits with a squared cross-sectional neck and a cavity with length and width dimensions $l_{\mathbf{n}}$ and $w_{\mathbf{n}}$, $l_{\mathbf{c}}$ and $w_{\mathbf{c}}$ respectively; or 3D (Figure 3.1(c)), made of square cross-sectional tubes, with neck and cavity widths w_n and w_c, and lengths l_n and l_c respectively. The system made by the slit with the loaded HRs (Figure 3.1(d)) is considered as the building block of the acoustic metamaterial described in this chapter.

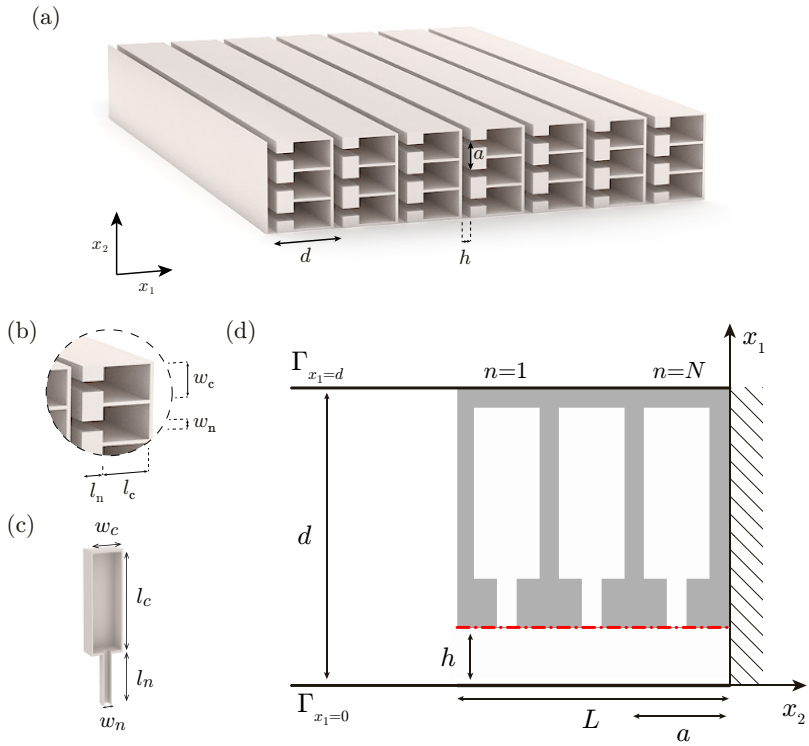


Figure 3.1. *(a) Conceptual view of the thin panel placed on a rigid wall with three layers of 2D Helmholtz resonators. (b) and (c) Conceptual views of 2D and 3D HRs respectively. (d) Scheme of the unit cell of the panel composed of a set of N Helmholtz resonators. Symmetry boundary conditions are applied at boundaries $\Gamma_{x_1=d}$ and $\Gamma_{x_1=0}$*

3.2.1. *Theoretical modeling: transfer-matrix method*

The transfer matrix is used to relate the sound pressures and normal acoustic particle velocities at the beginning and at the end of each unit cell. The transfer matrix of the n-th unit cell, $\mathbf{T}^n$, of length L, extending from $x_2 = 0$ to $x_2 = L$ is written as

$$\begin{bmatrix} P^n \\ V^n \end{bmatrix}_{y=0} = \mathbf{T}^n \begin{bmatrix} P^n \\ V^n \end{bmatrix}_{y=L} = \begin{bmatrix} T_{11}^n & T_{12}^n \\ T_{21}^n & T_{22}^n \end{bmatrix} \begin{bmatrix} P^n \\ V^n \end{bmatrix}_{y=L} . \quad [3.1]$$

For an identical set of M resonators, the transfer matrix $\mathbf{T}^n$ is written as

$$\mathbf{T}^n = \begin{bmatrix} T_{11}^n & T_{12}^n \\ T_{21}^n & T_{22}^n \end{bmatrix} = \mathbf{M}_{\Delta l_{\text{slit}}}^n \left(\mathbf{M}_{\mathbf{s}}^n \mathbf{M}_{\text{HR}}^n \mathbf{M}_{\mathbf{s}}^n\right)^M .$$

Here, the transfer matrix for each lattice step in the n-th slit, $\mathbf{M}_{\mathbf{s}}^n$, is written as

$$\mathbf{M}_{\mathbf{s}}^n = \begin{bmatrix} \cos\left(k_{\mathbf{s}}^n \frac{a}{2}\right) & iZ_{\mathbf{s}}^n \sin\left(k_{\mathbf{s}}^n \frac{a}{2}\right) \\ \frac{i}{Z_{\mathbf{s}}^n} \sin\left(k_s^n \frac{a}{2}\right) & \cos\left(k_{\mathbf{s}}^n \frac{a}{2}\right) \end{bmatrix}, \quad [3.2]$$

where the slit characteristic impedance is written as $Z_{\mathbf{s}}^n = \sqrt{\kappa_{\mathbf{s}}^n \rho_{\mathbf{s}}^n}/S_{\mathbf{s}}^n$ and $S_{\mathbf{s}}^n$ is equal to h^n in the 2D HRs and equal to $h^n\, a$ in the 3D HRs. The resonators are introduced as punctual scatters by a transfer matrix $\mathbf{M}_{\text{HR}}^n$ as

$$\mathbf{M}_{\text{HR}}^n = \begin{bmatrix} 1 & 0 \\ 1/Z_{\text{HR}}^n & 1 \end{bmatrix}, \quad [3.3]$$

and the radiation correction of the n-th slit to the free space as

$$\mathbf{M}_{\Delta l_{\text{slit}}}^n = \begin{bmatrix} 1 & Z_{\Delta l_{\text{slit}}}^n \\ 0 & 1 \end{bmatrix}, \quad [3.4]$$

with the characteristic radiation impedance of the n-th slit $Z_{\Delta l_{\text{slit}}}^n = -i\omega \Delta l_{\text{slit}}^n \rho_0/\phi_t^n S_0$, where S_0 is equal to d for 2D and equal to $d\, a$ for 3D, ρ_0 is the air density and Δl_{slit}^n is the proper end correction that will be described later.

The reflection coefficient of the rigidly backed slit can be directly calculated from the elements of the matrix $\mathbf{T}^n$ as

$$R^n = \frac{T_{11}^n - Z_0 T_{21}^n}{T_{11}^n + Z_0 T_{21}^n}. \qquad [3.5]$$

with $Z_0 = \rho_0 c_0 / S_0$, and finally the absorption as $\alpha^n = 1 - |R^n|^2$.

Finally, the effective parameters of each slit can be obtained from the transfer-matrix elements as follows:

$$k_{\text{eff}}^n = \frac{1}{L}\cos^{-1}\left(\frac{T_{11}^n + T_{22}^n}{2}\right), \quad Z_{\text{eff}}^n = \sqrt{\frac{T_{12}^n}{T_{21}^n}}. \qquad [3.6]$$

In the case of different HRs, the total transfer matrix of the whole system can be obtained by the product of the transfer matrices of each layer of the material. Thus, the total transfer-matrix method of the system is given by

$$\mathbf{T}^n = \begin{bmatrix} T_{11}^n & T_{12}^n \\ T_{21}^n & T_{22}^n \end{bmatrix} = \mathbf{M}_{\Delta l_{\text{slit}}}^n \prod_{m=1}^{M} \left(\mathbf{M}_{\mathbf{s}}^n \mathbf{M}_{\text{HR}}^{n,m} \mathbf{M}_{\mathbf{s}}^n\right).$$

where the matrix $\mathbf{M}_{\text{HR}}^{n,m}$ is calculated for each m resonator in each n slit.

3.2.1.1. *Viscothermal losses model*

The viscothermal losses in the system are considered in both the HRs and in the slits by using its effective complex and frequency-dependent parameters. Considering that only plane waves propagate inside the metamaterial, the effective parameters of the ducts that conform 2D resonators and the slits of width w are given by [STI 91]:

$$\rho_{\text{eff}} = \rho_0 \left[1 - \frac{\tanh\left(\frac{w}{2}G_\rho\right)}{\frac{w}{2}G_\rho}\right]^{-1}, \qquad [3.7]$$

$$\kappa_{\text{eff}} = \kappa_0 \left[1 + (\gamma - 1)\frac{\tanh\left(\frac{w}{2}G_\kappa\right)}{\frac{w}{2}G_\kappa}\right]^{-1}, \qquad [3.8]$$

with $G_\rho = \sqrt{i\omega\rho_0/\eta}$ and $G_\kappa = \sqrt{i\omega \text{Pr}\rho_0/\eta}$, and where γ is the specific heat ratio of air, P_0 is the atmospheric pressure, Pr is the Prandtl number, η is the dynamic viscosity, ρ_0 is the air density and $\kappa_0 = \gamma P_0$ is the air bulk modulus. The effective parameters of the n-th main slit, $\rho_{\mathbf{s}}^n$ and $\kappa_{\mathbf{s}}^n$, are obtained by setting $w = h^n$ in equations [3.7–3.8]. The viscothermal losses inside the two-dimensional resonators neck and cavity are modeled in the same way by these effective parameters, $\rho_{\mathbf{n}}^{n,m}$,

$\kappa_{\mathbf{n}}^{n,m}$ and $\rho_{\mathbf{c}}^{n,m}$, $\kappa_{\mathbf{c}}^{n,m}$ respectively, by setting $w = w_{\mathbf{n}}^{n,m}$ and $w = w_{\mathbf{c}}^{n,m}$ for the m-th resonator located at the n-th slit.

In the case of 3D HRs, the propagation in a rectangular cross-sectional tube can be described by its complex and frequency-dependent density and bulk modulus, and considering that plane waves propagate inside can be expressed as [STI 91]:

$$\rho_t = -\frac{\rho_0 a^2 b^2}{4G_\rho^2 \sum_{k\in\mathbb{N}} \sum_{m\in\mathbb{N}} \left[\alpha_k^2\beta_m^2\alpha_k^2 + \beta_m^2 - G_\rho^2\right]^{-1}}\,, \qquad [3.9]$$

$$\kappa_t = \frac{\kappa_0}{\gamma + \frac{4(\gamma-1)G_\kappa^2}{a^2b^2} \sum_{k\in\mathbb{N}} \sum_{m\in\mathbb{N}} \left[\alpha_k^2\beta_m^2\alpha_k^2 + \beta_m^2 - G_\kappa^2\right]^{-1}}\,, \qquad [3.10]$$

with the constants $\alpha_k = 2(k+1/2)\pi/a$ and $\beta_m = 2(m+1/2)\pi/b$, and the dimensions of the duct a and b being either the neck, $a = b = w_n$ or the cavity, $a = b = w_c$ of the HRs.

3.2.1.2. *Resonator impedance and end corrections*

Using the effective parameters for the neck and cavity elements given by equations [3.7–3.8], the impedance of a Helmholtz resonator, including a length correction due to the radiation can be written as [THE 14]:

$$Z_{\mathrm{HR}}^{n,m} = -\imath\frac{c_n c_c - Z_n k_n \Delta l c_n s_c/Z_c - Z_n s_n s_c/Z_c}{s_n c_c/Z_n - k_n \Delta l s_n s_c/Z_c + c_n s_c/Z_c}\,, \qquad [3.11]$$

where $c_n = \cos(k_n l_n)$, $c_c = \cos(k_c l_c)$, $s_n = \sin(k_n l_n)$, $s_c = \sin(k_c l_c)$ in which note superscripts were omitted for the sake of simplicity. $l_{\mathbf{n}}^{n,m}$ and $l_{\mathbf{c}}^{n,m}$ are the neck and cavity lengths, $k_{\mathbf{n}}^{n,m}$ and $k_{\mathbf{c}}^{n,m}$ are the effective wavenumbers, $Z_{\mathbf{n}}^{n,m}$ and $Z_{\mathbf{c}}^{n,m}$ are the effective characteristic impedance in the neck and cavities respectively, and $\Delta l^{n,m}$ is the correction length for the HRs. These correction lengths are deduced from the addition of two correction lengths $\Delta l^{n,m} = \Delta l_1^{n,m} + \Delta l_2^{n,m}$ as

$$\Delta l_1^{n,m} = 0.41\left[1 - 1.35\frac{w_{\mathbf{n}}^{n,m}}{w_{\mathbf{c}}^{n,m}} + 0.31\left(\frac{w_{\mathbf{n}}^{n,m}}{w_{\mathbf{c}}^{n,m}}\right)^3\right] w_{\mathbf{n}}^{n,m}\,, \qquad [3.12]$$

$$\Delta l_2^{n,m} = 0.41\Big[1 - 0.235\frac{w_{\mathbf{n}}^{n,m}}{w_{\mathbf{s}}^{n}} - 1.32\left(\frac{w_{\mathbf{n}}^{n,m}}{w_{\mathbf{s}}^{n}}\right)^2 + 1.54\left(\frac{w_{\mathbf{n}}^{n,m}}{w_{\mathbf{s}}^{n}}\right)^3 - 0.86\left(\frac{w_{\mathbf{n}}^{n,m}}{w_{\mathbf{s}}^{n}}\right)^4\Big] w_{\mathbf{n}}^{n,m}\,. \qquad [3.13]$$

The first length correction, $\Delta l_1^{n,m}$, is due to pressure radiation at the discontinuity from the neck duct to the cavity of the Helmholtz resonator [KER 87], while the second correction, $\Delta l_2^{n,m}$, comes from the radiation at the discontinuity from the neck to the principal waveguide [DUB 99]. This correction only depends on the radius of the waveguides, so it becomes important when the duct length is comparable to the radius, i.e. for small neck lengths and for frequencies where $k_{\mathbf{n}}^{n,m} w_{\mathbf{n}}^{n,m} \ll 1$.

Another important end correction comes from the radiation from the slits to the free air. The radiation correction for a periodic distribution of slits can be expressed as [MEC 08]:

$$\Delta l_{\text{slit}}^n = h^n \sigma^n \sum_{n=1}^{\infty} \frac{\sin^2(n\pi\sigma^n)}{(n\pi\sigma^n)^3}. \qquad [3.14]$$

with $\sigma^n = h^n/d$. Note for $0.1 \leq \sigma^n \leq 0.7$, this expression reduces to $\Delta l_{\text{slit}}^n \approx -\sqrt{2}\ln\left[\sin \pi\sigma^n/2\right]/\pi$.

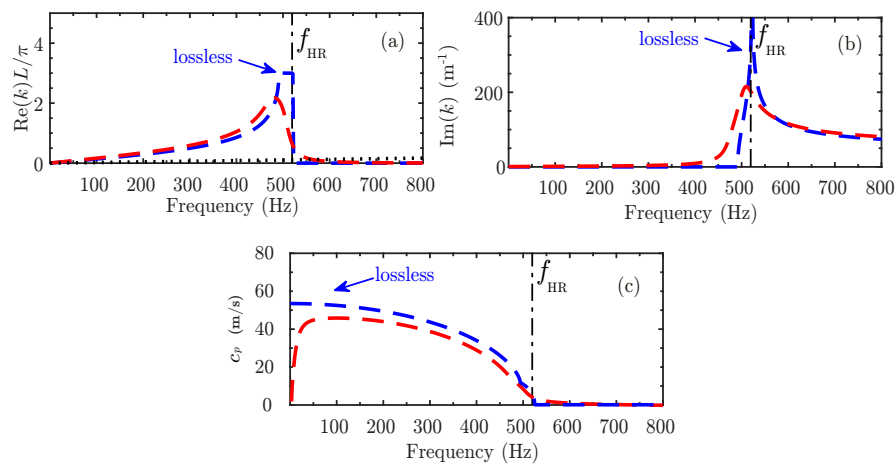


Figure 3.2. *(a) and (b) Real and imaginary parts of the dispersion relation calculated by the TMM for a metamaterial with parameters $h = 1.2$ mm, $a = 1.2$ cm, $w_n = a/6$, $w_c = a/2$, $d = 7$ cm, $l_n = d/3$ and $l_c = d - h - l_n$. Blue lines represent the lossless case, while red lines represent the lossy case. Black dotted lines represent the dispersion relation of the main slit without HRs. (c) Phase speed calculated by TMM for the lossless case (blue) and including thermo-viscous losses (red). For a color version of this figure, see www.iste.co.uk/romero/metamaterials.zip*

3.2.2. *Infinite main slit: dispersion relation and slow sound effect*

We first consider the dispersion properties inside the unit cell. In order to do that we consider a unit cell made of an infinite number of resonators with periodicity a. In this case, by applying periodic boundary conditions in a single periodicity of the unit cell, we can evaluate the dispersion relation inside the main slit with the presence of the resonators. Figure 3.2(a) and (b) show the real and imaginary parts of the dispersion relation calculated by the TMM for both the lossless and lossy cases. The first feature of this dispersion relation is that a bandgap can be observed above the resonant frequency of the HRs, f_{HR}. Below the resonance frequency of the HRs, a dispersive band is observed and the wavenumber is increased with respect to the wavenumber in air. Note also that the maximum wavenumber inside the slit is limited by the discreteness to the value $k_{\max} = \pi N/L$, as shown by the TMM calculations (dashed blue curve in Figure 3.2(b)). Interestingly, the imaginary part of this dispersion relation in the lossy case becomes important around the resonance frequency even in the case where the real part of the dispersion relation is not in the bandgap. However, the losses are less important when we are far from the resonant frequency of the HRs, f_{HR}.

Figure 3.2(c) shows the real part of the phase velocity in the slit, calculated both in the lossless and lossy cases. In this regime, slow sound conditions are produced due to the strong dispersion introduced by the resonators. In the lossless case, zero phase velocity can be observed for frequencies just below f_{HR}. In the lossy case, the losses limit the minimum value of the group velocity [THE 14]; however, in our system, slow sound velocity can be achieved in the dispersive band below f_{HR}. The average sound speed in the low frequency range is much lower (50 m/s) than the speed of sound in air (black dotted line in the main slit).

3.2.3. *Finite slits*

In reality, the unit cells used in the analyzed acoustic metamaterials will be of finite size, therefore, in general we will use the scattering matrix of the unit cells in order to study the scattering properties of the system. In particular, in the problems analyzed in this chapter, i.e. in the reflection problems, the reflection coefficient which represents the scattering coefficient of the system is of particular interest. In this section, we show the different possibilities for tuning this reflection coefficient with finite unit cells.

3.2.3.1. *Managing the amplitude of the reflection coefficient: critical coupling condition*

In the complex frequency plane, the reflection coefficient has pairs of zeros and poles that are complex conjugates one from another in the lossless case. In the $\exp(-\imath\omega t)$ sign convention, the zeros are located in the positive imaginary plane. The imaginary part of the complex frequency of the poles of the reflection coefficient represents the energy leakage of the system into the free space [ROM 16a]. Once the intrinsic losses are introduced in the system, the zeros of the reflection coefficient move downwards to the real frequency axis [ROM 16b]. For a given frequency, if the intrinsic losses perfectly balance the energy leakage of the system, a zero of the reflection coefficient is exactly located on the real frequency axis and therefore perfect absorption, $\alpha = 1 - |R|^2 = 1$, can be obtained. This condition is known as the critical coupling [ROM 16a, ROM 16b, BLI 08, PIP 14, YAN 15, MA 14].

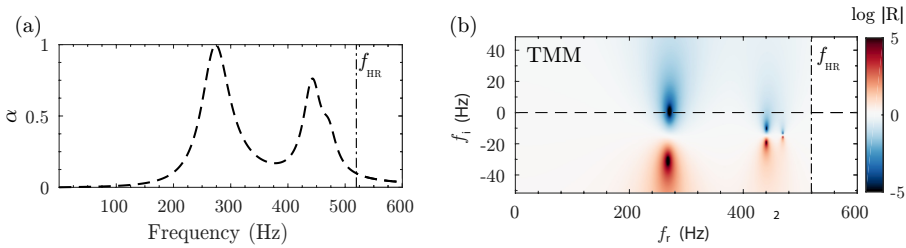


Figure 3.3. *(a) Absorption of a panel made of $N = 3$ resonators calculated by the TMM. The dashed-dotted line marks the resonant frequency of the HRs. (b) Complex frequency planes of the reflection coefficient calculated by TMM where f_r and f_i are the real and imaginary parts of the complex frequency respectively. For a color version of this figure, see www.iste.co.uk/romero/metamaterials.zip*

Figure 3.3(a) shows the absorption predicted by the TMM when the geometry of the system has been tuned to introduce the exact amount of intrinsic losses that exactly compensates the energy leakage of the system at 275 Hz for $N = 3$. In this situation, as shown in Figure 3.3(b), the lower frequency zero is located on the real axis, leading to a peak of perfect absorption. In addition, as we have $N = 3$ resonators, two other secondary peaks of absorption are observed at higher frequencies, for example 442 Hz and 471 Hz. Their corresponding zeros are located close to the real axis and, although the critical coupling condition is not exactly fulfilled, high absorption values can be observed at these frequencies. By using these concepts of slow sound and critical coupling, we theoretically and experimentally show in section 3.3 the possibilities of an acoustic metamaterial panel with deep subwavelength thickness for perfect and omnidirectional absorption.

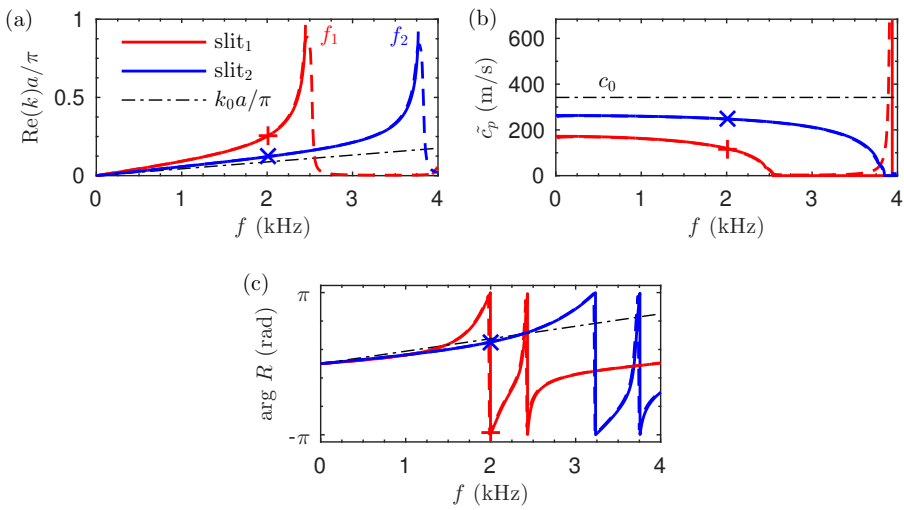


Figure 3.4. *(a) Dispersion relation inside the (blue) first and (red) second slits of a metadiffuser for the lossless case (continuous lines) and accounting for the thermo-viscous losses (dashed lines), and wavenumber in air (dashed-dotted). The resonance frequencies of the HR are shown as f_1 and f_2. (b) Corresponding phase speed. (c) Phase of the reflection coefficient for each individual slit. Image reproduced from [JIM 17a]. For a color version of this figure, see www.iste.co.uk/romero/metamaterials.zip*

3.2.3.2. *Managing the phase of the reflection coefficient*

Figure 3.4(a) shows the dispersion relations inside two different slits, $n = 1$ and $n = 2$, obtained by using HRs with the geometrical parameters listed in Table 3.2. Far from the resonance frequency, at the frequency marked by the symbols in Figure 3.4(a) and (b), the effect of losses is negligible as seen in the previous section 3.2.2. If now we consider a finite slit made of $M = 2$ resonators, due to the different slow sound velocity in the different slit, the phase of the reflection coefficient of each slit can be easily tuned by modifying the properties of the HRs. The phase of the reflection coefficient produced by each finite slit is shown in Figure 3.4(c). We can see that for some frequencies, the phase of the reflection coefficient of both slits (blue and red lines) is strongly modified when compared to the reflection phase of a slit without HRs (dashed line). At 2 kHz, the first slit (red curve) reacts inverting the phase of the incoming wave, while for the second slit (blue curve), this occurs at 3.2 kHz.

In this way, by tuning the geometry of the unit cell, a specific phase profile can be tailored, while the total thickness of the panel can be greatly reduced when compared with a quarter wavelength resonator of length L. By using these features, we will show in section 3.4 that the phase profile of Schroeder diffusers can be mimicked by a subwavelength metadiffuser in a given frequency band. Therefore, by tuning the geometry of a metadiffuser, we can maximize sound diffusion in a broad frequency band for room acoustics applications using a deep subwavelength panel.

3.3. Ultra-thin acoustic metamaterial absorbers

3.3.1. *Monochromatic frequency absorber*

In section 3.2.3.1, the critical coupling conditions have been used to design a perfect absorber for a thickness of $L = 3a = \lambda/34.5$. In this section, we will go further and, by using an optimization method (sequential quadratic programming (SQP) method [POW 78]), the geometry of the system will be tuned in order to minimize the thickness of the material, providing structures with perfect absorption and deep subwavelength dimensions.

The TMM was used in the optimization to consider the discreteness effects on the reflection coefficient. The resulting structure from the optimization procedure is shown in Figure 3.5(a): a sample with a single layer of resonators, $N = 1$ with $h = 2.63$ mm, $d = 14.9$ cm, $a = L = d/13 = 1.1$ cm, $w_n = 2.25$ mm, $w_c = 4.98$ mm, $l_n = 2.31$ cm and $l_c = 12.33$ cm. The width of the impedance tube used for measurements, d, makes it possible to fit 13 resonators in the transversal dimension as shown Figure 3.5(a). The sample was built using stereolithography techniques using a photosensitive epoxy polymer (Accura 60®, 3D Systems Corporation, Rock Hill, SC 29730, USA), where the acoustic properties of the solid phase are $\rho_0 = 1210$ kg/m^3, $c_0 = [1570, 1690]$ m/s. The structure presents a peak of perfect absorption at $f = 338.5$ Hz (different from that of the HR, $f_{\mathrm{HR}} = 370$ Hz) with a thickness $L = \lambda/88$.

Figure 3.5(b) shows the absorption coefficient at normal incidence calculated with the TMM, predicted numerically by FEM and measured experimentally. At $f = 338.5$ Hz, perfect absorption can be observed. The maximum absorption measured experimentally was $\alpha = 0.97$, as shown in the inset of Figure 3.5(b). This small discrepancy between the measurements and the models can be caused by experimental reasons including the non-perfect fitting of the slit on the impedance tube and the excitation of plate modes of the solid medium that composes the metamaterial.

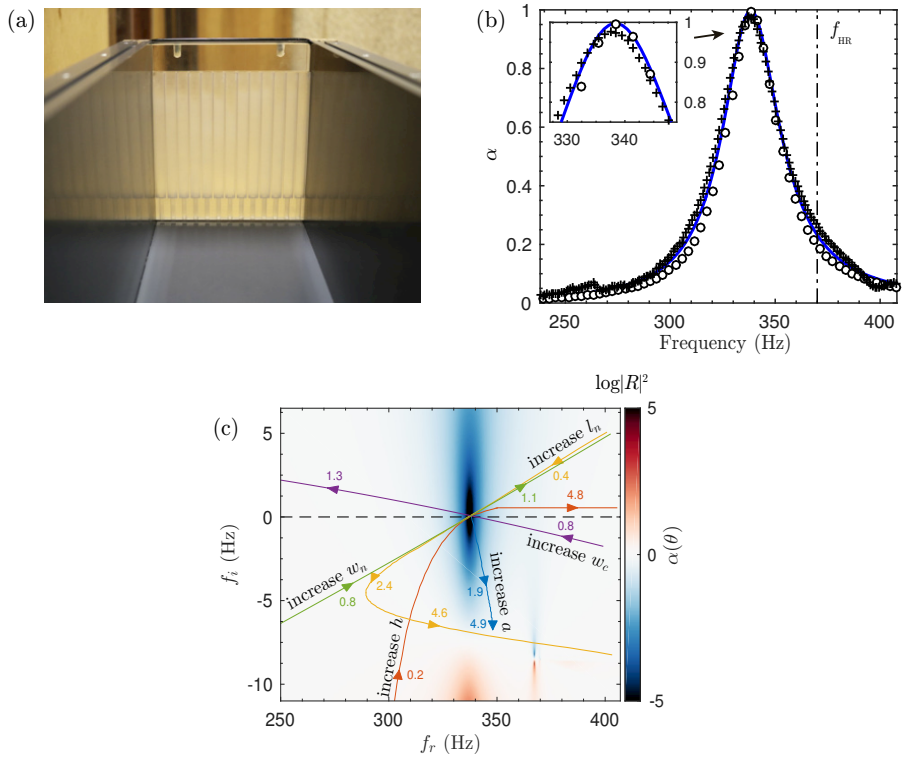


Figure 3.5. *(a) Photograph of the experimental setup with a vertical unit cell, $N = 1$, in the interior of the impedance tube. The translucent resin makes it possible to see the array of HRs. Picture shows the tube open, but it was closed for the experiments. (b) Absorption of the system measured experimentally (crosses), calculated by the transfer-matrix method (continuous blue) and finite element method (circles). (c) Representation of the reflection coefficient in the complex frequency plane for the optimized sample. Each line shows the trajectory of its zero by changing a geometry parameter. For a color version of this figure, see www.iste.co.uk/romero/metamaterials.zip*

On the contrary, Figure 3.5(c) shows the corresponding reflection coefficient in the complex frequency plane. The color map corresponds to the case in which the critical coupling condition is fulfilled, i.e. the zero of the reflection coefficient is exactly located on the real frequency axis. As long as the intrinsic losses depend on the geometry of the resonators and the thickness of the slits, we also represent in Figure 3.5(c) the trajectory of this zero as the geometry of the system is modified. The crossing of the trajectories with the real frequency axis implies that perfect absorption can be achieved with this system at this particular frequency. It can be

seen that the trajectories linked to the resonators' geometry, w_n, w_c, l_n have a strong effect in the real part of the complex frequency of the zero, as they modify the HRs' resonant frequency. In the case of l_n, due to the geometric constraint $d \geq h + l_n + l_c$, increasing the length of the neck also implies the reduction in the cavity and the trajectory of the zero is twisted. The trajectory of the slit thickness, h, shows that the intrinsic losses are excessively increased for very narrow slits and the critical coupling condition cannot be fulfilled. For very wide slits, the geometrical constraints also imply the reduction in the size of the resonators and therefore the resonant frequency is increased. Finally, the trajectory linked to the lattice size, a, shows how the depth of the slit, $L = Na$, is mainly linked to the intrinsic losses of the system: the peak absorption frequency is almost independent of a, it mostly depends on the resonator resonant frequency. Moreover, as the slow sound conditions are caused by the local resonance of the HRs, the periodicity of the array of HRs is not a necessary condition for these perfect absorbing panels. However, considering periodicity allows us to design and tune the system using the present analytical methods.

Finally, Figure 3.6 shows the absorption of the metamaterial panel as a function of the angle of incidence. It can be observed that almost perfect absorption is obtained for a broad range of angles, being $\alpha > 0.90$ for incident waves with $\theta < 60°$. The inset of Figure 3.5 shows the absorption in diffuse field [COX 09] calculated as $\alpha_{\text{diff}} = 2\int_0^{\pi/2} \alpha(\theta)\cos(\theta)\sin(\theta)\mathrm{d}\theta$ where, at the working frequency, it reaches a value of $\alpha_{\text{diff}} = 0.93$, showing the quasi-omnidirectional behavior of the absorption in this subwavelength structure.

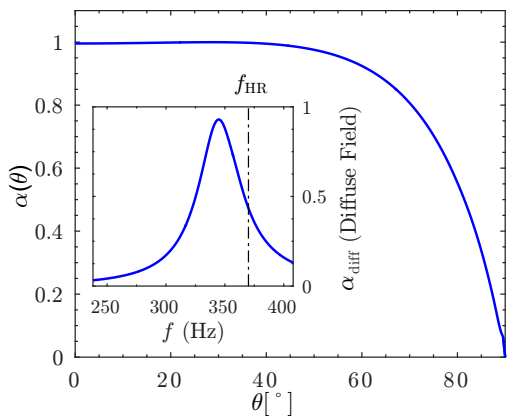


Figure 3.6. *Absorption peak as a function of the angle of incidence calculated by the transfer-matrix method (continuous blue). The inset shows the absorption coefficient in diffuse field as a function of frequency*

3.3.2. *Rainbow-trapping absorber*

Perfect acoustic absorption has been reported in the previous section by means of rigidly backed subwavelength structures by using slow sound and HRs. The interest now is focused on developing perfect and broadband absorption. When the system is not rigidly backed and transmission is allowed, obtaining perfect absorption becomes challenging because the scattering matrix of the system presents two different eigenvalues. In order to obtain perfect absorption, both eigenvalues must vanish at the same frequency [MER 15]. This implies that symmetric and antisymmetric modes must be simultaneously critically coupled at a given frequency [PIP 14]. When the eigenvalues are both zero but at different frequencies, then the system cannot present perfect absorption, but quasi-perfect absorption can be achieved by approaching the symmetric and antisymmetric modes using strong dispersion [JIM 17d]. Perfect acoustic absorption in transmission problems can be obtained by using degenerate resonators, exciting a monopolar and a dipolar mode at the same frequency [YAN 15]. Using elastic membranes decorated with designed patterns of rigid platelets [MEI 12], very selective low-frequency perfect absorption can be observed. Another strategy consists of using asymmetric graded materials, e.g. chirped layered porous structures [JIM 16b], but these structures' lack of subwavelength resonances and therefore their thickness is of the order of half of the incoming wavelength. A final configuration to achieve perfect absorption in transmission consists of breaking the symmetry of the structure by making use of double-interacting resonators, after which perfect absorption was observed in waveguides at a particular frequency [MER 15].

In this section, we address the problem of perfect and broadband acoustic absorption using deep subwavelength structures in non-rigidly backed panels by extending the results shown in the previous section. To do so, we design panels composed of monopolar resonators with graded dimensions, namely *rainbow-trapping absorbers*, as shown in Figure 3.7(a). The rainbow-trapping phenomenon, i.e. the localization of energy due to a gradual reduction of the group velocity in graded structures, has been observed in optics [TSA 07], acoustics [ZHU 13, ROM 13] and elastodynamics [COL 16]. However, losses were not accounted for and therefore absorption was not studied in these works. In the present configuration, a set of graded HRs are used, allowing one to reduce, in addition to the thickness of the panels, the dimension of the unit cell to the deep subwavelength regime. In particular, the structures are composed of a rigid panel, of thickness L, periodically perforated with series of identical waveguides of variable square cross-section loaded by an array of N HRs of different dimensions, as shown in Figure 3.7(a and b). Each waveguide is therefore divided into N segments of length $a^{[n]}$, width $h_1^{[n]}$ and height $h_3^{[n]}$. The HRs are located in the middle of each waveguide section. The *rainbow-trapping absorber* (RTA) was composed of $N = 9$ HRs for the experimental tests, as shown in Figure 3.7(b). The geometrical parameters of both

structures were tuned using optimization methods (sequential quadratic programming (SQP) [POW 78]). In the case of the rainbow-trapping absorber, the cost function was $\varepsilon_{\mathrm{RTA}} = \int_{f_1}^{f_N} |R^-|^2 + |T|^2 df$, i.e. to maximize the absorption in a broad frequency bandwidth, which was chosen from $f_1 = 300$ to $f_N = 1000$ Hz. In the case of the RTA, the length of the panel was constrained to $L = 11.3$ cm, i.e. a panel 10 times thinner than the wavelength at 300 Hz. The geometrical parameters for the RTA $(N = 9)$, measured experimentally, corresponding to Figure 3.7(b), are listed in Table 3.1. The total structure thickness is $L = \sum a^{[n]} = 113$ mm, and its height and the width of the unit cell are $d_3 = 48.7$ mm and $d_1 = 14.6$ mm respectively.

The idea here is to create a frequency-cascade of bandgaps and critically coupled resonators in order to generate a rainbow-trapping effect. The process is as follows: first, we tune the deepest resonator $(n = 1)$ in the waveguide to reduce the transmission above a frequency f_1; second, a second resonator with slightly higher resonance frequency, f_2, is placed in the preceding segment of the waveguide. The geometry of this resonator and the section of the waveguide are tuned to impedance match the system at this frequency. Therefore, the reflection vanishes and a peak of perfect absorption is achieved in the same way as in the previous section. Note that the latter HR also reduces the transmission at even higher frequencies. Thus the process can be repeated by extending the waveguide with more segments, each one with a tuned HR with a resonance frequency higher than the preceding one.

Following this process, a rainbow-trapping absorber is designed using $N = 9$ resonators. Due to machine precision of the available 3D printing system (the minimum step was 0.1 mm), the optimal RTA cannot be accurately manufactured. The main limitation is related to the loss of accuracy of the diameters of the small necks that compose the HRs. Under this technological constraint, we design an RTA using $N = 9$ HRs and quantizing the dimensions of all the geometrical elements that compose the structure to the machine precision. The manufactured sample is shown in Figure 3.7(b) and the quantized geometrical parameters are listed in Table 3.1. Figure 3.7(c–d) show the absorption, reflection and transmission of the device calculated with the TMM, FEM and measured experimentally. Note that both reflection and transmission coefficients are plotted in terms of amplitude and not in terms of energy in order to emphasize the fact that the transmission does not vanish apart from the perfect absorption frequency band. The deepest resonator $(n = 1)$ presents a resonance frequency of $f_1 = f_{\mathrm{gap}} = 259$ Hz, causing the transmission to drop. A set of nine resonators were tuned following the process previously described, with increasing resonance frequencies ranging from 330 to 917 Hz. As a result of the frequency-cascade process, the impedance of the structure in the working frequency range is matched with the exterior medium while the transmission vanishes. As a result, the RTA presents a flat and quasi-perfect absorption coefficient in this frequency range (see Figure 3.7(c)). Excellent agreement is found between the TMM

predictions and FEM simulations, while good agreement is observed between the experimental measurements and both models. It can be observed that at low frequencies, there are small differences between the measurements and the models. These disagreements are mainly caused by imperfections in the sample manufacturing, by imperfect fitting of the structure to the impedance tube, by the possible evanescent coupling between adjacent waveguides and adjacent HRs, and/or by the limitations of the viscothermal model used at the joints between waveguide sections.

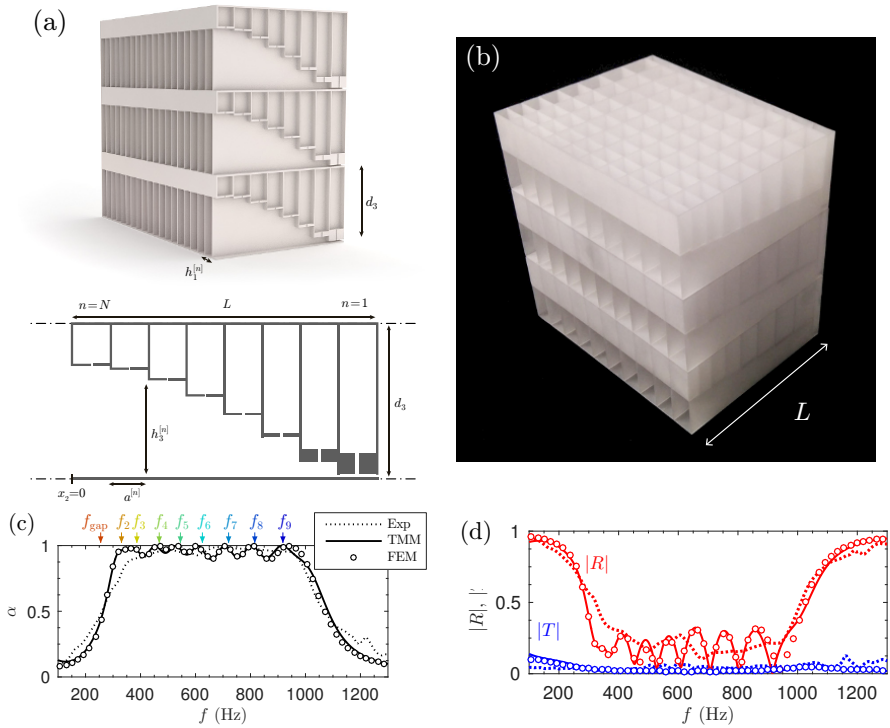


Figure 3.7. *(a) Conceptual view of a rainbow-trapping absorber (RTA) with $N = 8$ HRs. Scheme showing the geometrical variables for RTA. (b) Photograph of the sample containing 10×3 unit cells. (c) Absorption obtained by using the TMM (continuous line), FEM simulations (circles) and measured experimentally (dotted line). (d) Corresponding reflection (red curves) and transmission (blue curves) coefficients in amplitude. For a color version of this figure, see www.iste.co.uk/romero/metamaterials.zip*

n	$a^{[n]}$ (mm)	$h_3^{[n]}$ (mm)	$h_1^{[n]}$ (mm)	$l_{\mathbf{n}}^{[n]}$ (mm)	$l_{\mathbf{c}}^{[n]}$ (mm)	$w_{\mathbf{n}}^{[n]}$ (mm)	$w_{\mathbf{c},1}^{[n]}$ (mm)	$w_{\mathbf{c},2}^{[n]}$ (mm)
9	7.9	25.6	14.0	1.1	21.4	1.2	14.0	7.2
8	9.5	24.2	14.0	1.0	22.8	1.2	14.0	9.0
7	11.0	22.8	14.0	1.7	23.6	1.4	14.0	10.6
6	12.6	21.6	14.0	0.7	25.9	1.0	14.0	12.0
5	14.1	20.2	14.0	1.5	26.5	1.2	14.0	13.6
4	15.7	18.8	14.0	1.1	28.3	1.0	14.0	15.2
3	17.3	17.4	14.0	1.6	29.2	1.0	14.0	16.8
2	18.8	16.0	14.0	1.1	31.2	0.8	14.0	18.4
1	6.4	1.0	1.0	3.0	44.7	0.6	14.0	5.6

Table 3.1. *Geometrical parameters for the RTA ($N = 9$). Table reproduced from [JIM 17c]*

3.4. Metadiffusers

The far-field polar pressure distribution can characterize the performance of a diffuser. For a finite panel of side $2b$, the far-field polar pressure distribution, $p_s(\theta)$, of a locally reacting reflecting surface with a spatially dependent reflection coefficient, $R(x)$, can be calculated using the Fraunhofer integral as [COX 94]

$$p_s(\theta) = \int_{-b}^{b} R(x) e^{jk_0 x \sin\theta} dx, \qquad [3.15]$$

where θ is the polar angle and k_0 is the wavenumber in air. Note that the scattered pressure in the far-field is essentially a Fourier transform of the reflected field along the surface. Therefore, structures whose reflection coefficient distributions present a uniform magnitude Fourier transform with good sound diffusion properties [SCH 75].

The diffusion coefficient [ISO 12], d_ϕ, is estimated from a polar response as

$$\delta_\phi = \frac{\left(\int_{-\pi}^{\pi} I_s(\theta) d\theta\right)^2 - \int_{-\pi}^{\pi} I_s(\theta)^2 d\theta}{\int_{-\pi}^{\pi} I_s(\theta)^2 d\theta}, \qquad [3.16]$$

where $I_s(\theta)$ is the polar scattering intensity for a wave with incident angle ϕ. This coefficient is normalized to that of a plane reflector, δ_{flat}, to eliminate the effect of the finite size of the structure as $\delta_n = (\delta_\phi - \delta_{\text{flat}})/(1 - \delta_{\text{flat}})$.

Based on the principles introduced in the section 3.2.3.2, we now present novel deep subwavelength diffusers based on acoustic metamaterials with deep subwavelength dimensions. The system works as follows: first, we consider a rigid

panel of finite length with a set of N slits; second, we modify the dispersion relations inside each slit by loading one of their walls with a set of HRs. The sound propagation in each slit becomes strongly dispersive and the sound speed inside it, c_p, can be drastically reduced. Each slit behaves effectively as a deep subwavelength resonator and, therefore, the effective depth of the slits can be strongly reduced as $L = c_p/4f$ holds. By tuning the geometry of the HRs and the thickness of the slits, the dispersion relations inside each slit can be modified. As a result, the phase of the reflection coefficient can be tailored along the surface, for example to those of a Schroeder phase grating diffuser. Furthermore, by tuning the thermo-viscous losses, which are inherent in the HRs and in the narrow slits, the leakage of the structure can be compensated by the intrinsic losses of the system and perfect absorption can be obtained. Thus, the magnitude of the reflection coefficient can be also tuned, and the behavior of the slits ranges from perfect reflectors to perfect absorbers. Perfect absorbing slits allow the design of ternary sequence diffusers [COX 06] for low frequencies.

3.4.1. *Quadratic residue metadiffusers*

The first numerical sequence mimicked is the one used in quadratic residue diffusers (QRD). The sequence is given by $s_n = n^2 \mathrm{mod} N$, where mod is the least non-negative remainder of the prime number N. If the phase grating diffuser is based on quarter wavelength resonators (wells), the depth of the wells is given by $L_n = s_n \lambda_0 / 2N$, where λ_0 is the design wavelength. Here, we use optimization methods, for example sequential quadratic programming [POW 78], to tune the geometry of the metamaterial so the spatially dependent reflection coefficient matched between the QR-metadiffuser and the QRD only at 2000 Hz. A QRD with $N = 5$ QRD, a total thickness of $L = 27.4$ cm and side $Nd = 35$ cm was designed for a frequency of 500 Hz. Due to the small lateral size of the panel, the response was evaluated at 2000 Hz considering six repetitions of the unit cell in order to clearly generate the characteristic N diffraction grating lobes of the QRD in the far-field. Figure 3.8(a–b) shows the phase and magnitude of the reflection coefficient along the surface the ideal QRD and a QR-metadiffuser of $L = 2$ cm thickness and $M = 2$ HRs of same lateral dimensions. The geometrical parameters for the metadiffuser are listed in Table 3.2 and a scheme of the panel is shown in Figure 3.8(c). Perfect agreement is found between the reflection coefficients of the QR-metadiffuser and the target phase grating QRD. Figure 3.8(g) shows the far-field calculation at 2000 Hz using equation [3.15] for both structures. Excellent agreement is obtained between the polar responses using the TMM. To validate the design, a full-wave numerical solution using the finite element method (FEM) and accounting for the thermo-viscous losses is also provided. The FEM numerical solution agrees with the theoretical prediction, although small discrepancies can be observed. They are caused first because the radiation corrections used in the TMM are only approximate and, second, because the evanescent coupling between near slits in the TMM is not considered while it is implicitly included in the FEM simulations. The near-field

pressure distributions are shown in Figure 3.8(d–f) for the QR-metadiffuser, the QRD and a reference flat surface of the same width, respectively. Excellent agreement is observed between both diffusers, where it is clear how the field is scattered in other directions rather than specular. The presented QR-metadiffuser is 17.1 times thinner than the QRD (34 times smaller than the QRD design wavelength (500 Hz) and 8.5 times smaller than the evaluation wavelength (2000 Hz)).

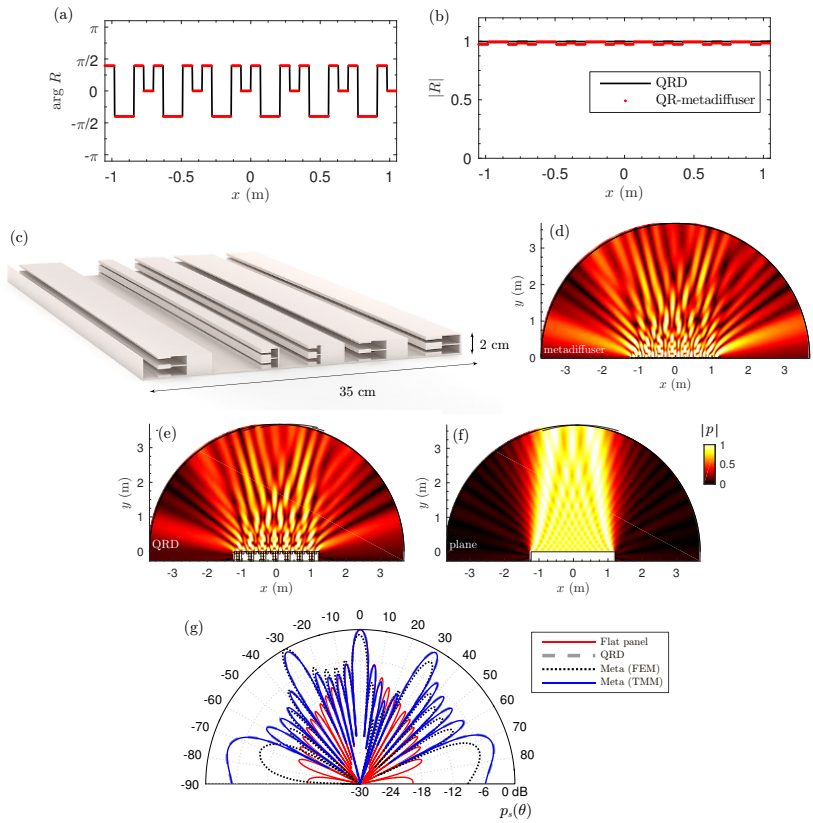


Figure 3.8. *(a) Phase and (b) magnitude of the spatially dependent reflection coefficient of a QRD (black line) and the QR-metadiffuser (red dotted line). (c) Scaled scheme of the QR-metadiffuser with $N = 5$ and $M = 2$. (d) Near-field pressure distribution at 2 kHz of QR-metadiffuser with thickness $L = 2$ cm, (e) phase grating QRD of thickness $L = 27.4$ cm and (f) flat plane reflector. (g) Far-field polar distribution of the QR-metadiffuser obtained by TMM (continuous blue) and FEM (dotted black), the reference QRD (dashed gray), and a plane reflector with same width of the diffusers (continuous red). For a color version of this figure, see www.iste.co.uk/romero/metamaterials.zip*

n	s_n	h (mm)	$l_\mathbf{n}$ (mm)	$l_\mathbf{c}$ (mm)	$w_\mathbf{n}$ (mm)	$w_\mathbf{c}$ (mm)
1	1.0	14.7	13.0	16.4	6.2	9.0
2	4.0	30.9	9.1	4.3	3.5	9.0
3	4.0	30.9	9.1	4.3	3.5	9.0
4	1.0	15.7	13.3	17.0	6.3	9.0
5	0.0	20.3	18.0	20.7	3.2	9.0

Table 3.2. *Geometrical parameters of the QR-metadiffuser. Table reproduced from [JIM 17a]*

3.4.2. *Broadband optimal metadiffusers*

To design a metadiffuser useful for room acoustics, its diffusion must be broad in frequency. Thus, we extended the bandwidth of the optimization procedure, where the cost function to minimize was $\varepsilon = 1 - \int_{f_{\text{low}}}^{f_{\text{high}}} \delta_n df$. In particular, we look for deep subwavelength thickness metadiffusers that present maximum normalized diffusion coefficient in the frequency range from $f_{\text{low}} = 250$ Hz to $f_{\text{high}} = 2000$ Hz. Here, we used a set of $N = 11$ slits separated by $d = 12$ cm, and constrained the thickness of the panel to $L = 3$ cm. The obtained geometrical parameters are listed in Table 3.3. Here, we used square cross-sectional HRs. Figure 3.9(a) shows the scheme of the metadiffuser with the retrieved geometry. First, the polar responses at two frequencies 300 and 2000 Hz are shown in Figure 3.9(b and c). The maximization of the diffusion coefficient implies that the polar responses are uniform. In addition, we show the angular dependence of the near field at shorter distances, for example at 1 and 5 m. Due to the lateral dimension of the structure, which is 1.32 m, equation [3.15] is not accurate at distances much shorter than the Rayleigh distance. However, although the near field does not exactly follow the polar distribution given by equation [3.15], the structure scatters the waves uniformly in broad range of angles when compared with a flat plane of the same dimensions. Figure 3.9(d–g) show the frequency-dependent polar responses in the far field for a reference flat plane with the same width as the metadiffuser, a thick QRD with a design frequency of 250 Hz ($L_{\text{QRD}} = 56$ cm), a thin QRD with the same thickness of the metadiffuser $L_{\text{QRD,thin}} = 3$ cm and the optimized metadiffuser, respectively. Here, we calculated the polar responses using six repetitions of the panel to clearly observe the diffraction grating lobes. First, the scattering of the thin QRD, Figure 3.9(e), is almost the same as a flat plane, Figure 3.9(d). It only starts to scatter waves at different angles above 2 kHz. Second, the deep wells that compose the thick QRD, Figure 3.9(f), resonate near their quarter-wavelength resonances at lower frequencies and, therefore, the

reflection coefficient follows the QR sequence and the panel scatters sound waves into oblique angles. Finally, the optimized metadiffuser, Figure 3.9(g), also shows strong grating lobes, but, in addition, at medium and high frequencies, energy is spread in other directions at low frequencies, for example between 250 and 500 Hz.

n	1	2	3	4	5	6	7	8	9	10	11
h (mm)	5.7	4.9	7.7	82.9	48.4	74.9	20.0	6.6	76.2	29.5	7.6
$l_{\mathbf{n}}$ (mm)	16.3	7.3	37.1	0.0	35.3	22.1	14.7	0.1	0.0	0.1	4.8
$l_{\mathbf{c}}$ (mm)	97.1	106.8	74.2	36.0	35.3	22.1	84.3	112.2	42.7	89.4	106.5
$w_{\mathbf{n}}$ (mm)	6.7	6.5	10.0	29.0	29.0	29.0	14.0	9.5	29.0	27.6	6.2
$w_{\mathbf{c}}$ (mm)	29.0	29.0	29.0	29.0	29.0	29.0	29.0	29.0	29.0	29.0	29.0

Table 3.3. *Geometrical parameters used for the broadband metadiffuser using N different slits. Table reproduced from [JIM 17a]*

The normalized diffusion coefficient shown in Figure 3.9(h) quantifies this behavior. It is observed that over the optimized range, the diffusion coefficient of the metadiffuser takes values with a mean value of about $\delta_n = 0.65$, with peaks of $\delta_n = 0.9$. When compared to the thick QRD, its frequency band is extended to one octave below. The corresponding absorption is shown in Figure 3.9(f). Here, the wide slits that form the QRD produce almost no losses, while the thermo-viscous losses produced in the narrow ducts that comprise the ultra-thin metamaterial lead to some peaks of absorption at the resonance of the cavities. These losses can be reduced if the thickness of the panel is increased, but here we presented a structure whose thickness is 46 times smaller than the wavelength. It is worth noting here that the size of some of neck of the resonators is almost the same as their cavities, as can be observed in Figure 3.9(a). In these cases, the resonator acts as a coiled QWR and the losses in these wide ducts are decreased. The resonance frequency of these QWR is higher than the corresponding HRs, contributing to the high frequency diffusion, while, in contrast, the HRs introduce spatial changes on the reflection coefficient at low frequencies. Moreover, the position of the low frequency absorption peaks can be engineered to solve other typical problems in room acoustics, as placing them at the resonant modes of small control rooms to produce a flatter spectral response or reduce sound coloration in the reverberation. This can be achieved using multi-objective optimization techniques.

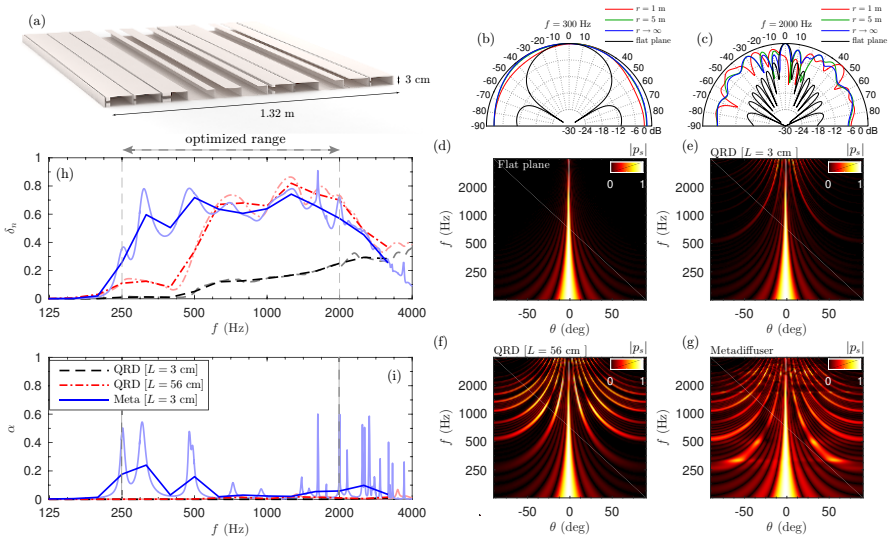


Figure 3.9. *(a) Scheme of the analyzed metadiffuser. (b) and (c) show the polar responses at two frequencies, 300 and 2000 Hz respectively. Far-field polar response as a function of the frequency for (d) reference flat plane, (e) $N = 11$ QRD panel with a total thickness of 3 cm, (f) QRD panel with a total thickness of 56 cm and (g) an optimized metadiffuser thickness of 3 cm. (h) Normalized diffusion coefficient or the 3 cm QRD (dashed black), 32 cm QRD (dashed-dotted red) and optimized metadiffuser using the TMM (blue) integrated in third of octaves. The third octave integration is shown in thick lines according to ISO 17497-2:2012 [ISO 12]. (i) Corresponding absorption. For a color version of this figure, see www.iste.co.uk/romero/metamaterials.zip*

3.5. Conclusions

Realistic panels for sound perfect absorption and diffusion with subwavelength sizes are designed in this chapter with simple structures made of bricks with Helmholtz resonators. The theoretical modeling based on the transfer-matrix method considering the viscothermal losses has been described in detail. Two examples of perfect absorbers and metadiffusers have been described.

Perfect absorption of sound is achieved at 338.5 Hz with a panel thickness of $L = \lambda/88 = 1.1$ cm and without added porous material. It is worth noting here that the total panel size in the vertical dimension is also subwavelength $d = \lambda/6.5 = 14.5$ cm. The subwavelength feature of the presented structure provides

perfect absorption for a wide range of incident angles. This almost omnidirectional sound absorber can be used in practical applications where the omnidirectional feature is mandatory. These promising results have been used to study different configurations producing broadband perfect absorption with deep subwavelength structures, named rainbow-trapping absorbers. We reported flat and perfect absorption over a frequency range covering from 300 to 1000 Hz, i.e. almost two octaves, using a rainbow-trapping absorber (RTA) composed of nine resonators and 10 times smaller than the wavelength at 300 Hz (11.3 cm).

Metadiffusers, a novel design of locally reacting surfaces with tailored acoustic scattering, were also presented. The propagation inside the metamaterial presents strong dispersion and the sound speed can be significantly reduced so that each slit effectively behaves as a deep subwavelength resonator. Thus, by tuning the material geometry, the dispersion of acoustic waves in the slits is modified and the spatially dependent reflection coefficient can be tailored to specific functions with a uniform magnitude Fourier transform. In these conditions, the grating lobes produced by a periodic arrangement of the panel all have the same energy. The acoustic energy can be scattered in other directions than specular. It was also shown that the structures can be optimized to work in a broad frequency range covering three octaves. In particular, we presented a diffuser of 3 cm thickness working from 250 to 2000 Hz, demonstrating the potential of the metadiffusers to be used in critical listening environments due to their deep subwavelength nature: the thickness of the panels was 1/46 to 1/20 times the design wavelength, i.e. between about a twentieth and a tenth of the thickness of traditional designs. In the context of smart building design and sustainability, metadiffusers can be used to save space and to produce lightweight materials, improving the performance of the acoustic solutions using less resources. Moreover, the proposed designs have the potential to meet the aesthetic requirements that are mandatory for modern auditoria design.

3.6. Acknowledgments

This work is based on work from COST Action DENORMS – CA15125, supported by COST (European Cooperation in Science and Technology). The authors acknowledge financial support from the Metaudible Project no. ANR-13-BS09-0003, cofounded by ANR and FRAE.

3.7. References

[ACH 16] ACHILLEOS V., RICHOUX O., THEOCHARIS G., "Coherent perfect absorption induced by the nonlinearity of a Helmholtz resonator", *Journal of the Acoustical Society of America*, vol. 140, no. 1, 2016.

[BLI 08] BLIOKH K.Y., BLIOKH Y.P., FREILIKHER V *et al.* "Unusual resonators: Plasmonics, metamaterials, and random media", *Reviews of Modern Physics*, vol. 80, no. 4, p. 1201, 2008.

[CAI 14] CAI X., GUO Q., HU G. *et al.*, "Ultrathin low-frequency sound absorbing panels based on coplanar spiral tubes or coplanar Helmholtz resonators", *Applied Physics Letters*, vol. 105, no. 12, p. 121901, 2014.

[COL 16] COLOMBI A., COLQUITT D., ROUX P. *et al.*, "A seismic metamaterial: The resonant metawedge", *Scientific Reports*, vol. 6, 2016.

[COX 94] COX T.J., LAM Y., "Prediction and evaluation of the scattering from quadratic residue diffusers", *Journal of the Acoustical Society of America*, vol. 95, no. 1, pp. 297–305, 1994.

[COX 06] COX T.J., ANGUS J.A., D'ANTONIO P., "Ternary and quadriphase sequence diffusers", *Journal of the Acoustical Society of America*, vol. 119, no. 1, pp. 310–319, 2006.

[COX 09] COX T.J., D'ANTONIO P., *Acoustic Absorbers and Diffusers: Theory, Design and Application*, CRC Press, Boca Raton, 2009.

[DUB 99] DUBOS V., KERGOMARD J., KHETTABI A. *et al.*, "Theory of sound propagation in a duct with a branched tube using modal decomposition", *Acta Acustica United With Acustica*, vol. 85, no. 2, pp. 153–169, 1999.

[GRO 15] GROBY J.-P., HUAND W., LARDEAU A. *et al.*, "The use of slow sound to design simple sound absorbing materials", *Journal of Applied Physics*, vol. 117, no. 124903, 2015.

[GRO 16] GROBY J.-P., POMMIER R., AURÉGAN Y., "Use of slow sound to design perfect and broadband passive sound absorbing materials", *Journal of the Acoustical Society of America*, vol. 139, no. 4, pp. 1660–1671, 2016.

[ISO 12] ISO 17497–2:2012, Acoustics – Sound-scattering properties of surfaces – Part 2: Measurement of the directional diffusion coefficient in a free field, ISO standard, International Organization for Standardization, Geneva, Switzerland, 2012.

[JIM 16a] JIMÉNEZ N., HUANG W., ROMERO-GARCÍA V. *et al.*, "Ultra-thin metamaterial for perfect and quasi-omnidirectional sound absorption", *Applied Physics Letters*, vol. 109, no. 121902, 2016.

[JIM 16b] JIMÉNEZ N., ROMERO-GARCÍA V., CEBRECOS A. *et al.*, "Broadband quasi perfect absorption using chirped multi-layer porous materials", *AIP Advances*, vol. 6, no. 12, p. 121605, 2016.

[JIM 17a] JIMÉNEZ N., COX T.J., ROMERO-GARCÍA V. *et al.*, "Metadiffusers: Deep-subwavelength sound diffusers", *Scientific Reports*, no. 7, p. 5389, 2017.

[JIM 17b] JIMÉNEZ N., GROBY J.-P., PAGNEUX V. *et al.*, "Iridescent perfect absorption in critically-coupled acoustic metamaterials using the transfer matrix method", *Applied Sciences*, vol. 7, no. 6, p. 618, 2017.

[JIM 17c] JIMÉNEZ N., ROMERO-GARCÍA V., PAGNEUX V. *et al.*, "Rainbow-trapping absorbers: Broadband, perfect and asymmetric sound absorption by subwavelength panels with transmission", *Scientific Reports*, no. 7, p. 135595, 2017.

[JIM 17d] JIMÉNEZ N., ROMERO-GARCÍA V., PAGNEUX V. *et al.*, "Quasiperfect absorption by subwavelength acoustic panels in transmission using accumulation of resonances due to slow sound", *Physical Review B*, vol. 95, p. 014205, 2017.

[JIM 18] JIMÉNEZ N., ROMERO-GARCÍA V., GROBY J.-P., "Perfect absorption of sound by Rigidly-Backed High-Porous materials", *Acta Acustica United with Acustica*, vol. 104, no. 3, pp. 396–409, 2018.

[KER 87] KERGOMARD J., GARCIA A., "Simple discontinuities in acoustic waveguides at low frequencies: Critical analysis and formulae", *Journal of Sound and Vibration*, vol. 114, no. 3, pp. 465–479, 1987.

[LI 16] LI Y., ASSOUAR B.M., "Acoustic metasurface-based perfect absorber with deep subwavelength thickness", *Applied Physics Letters*, vol. 108, no. 6, p. 063502, 2016.

[MA 14] MA G., YANG M., XIAO S. *et al.*, "Acoustic metasurface with hybrid resonances", *Nature Materials*, vol. 13, no. 9, pp. 873–878, 2014.

[MEC 08] MECHEL F.P., *Formulas of Acoustics*, 2nd edition, Springer Science & Business Media, Springer-Verlag, Berlin, Heidelberg, 2008.

[MEI 12] MEI J., MA G., YANG M. *et al.*, "Dark acoustic metamaterials as super absorbers for low-frequency sound", *Nature Communications*, vol. 3, p. 756, 2012.

[MER 15] MERKEL A., THEOCHARIS G., RICHOUX O. *et al.*, "Control of acoustic absorption in one-dimensional scattering by resonant scatterers", *Applied Physics Letters*, vol. 107, no. 24, p. 244102, 2015.

[PIP 14] PIPER J.R., LIU V., FAN S., "Total absorption by degenerate critical coupling", *Applied Physics Letters*, vol. 104, no. 25, p. 251110, 2014.

[POW 78] POWELL M.J., "A fast algorithm for nonlinearly constrained optimization calculations", *Numerical Analysis*, pp. 144–157, 1978.

[ROM 13] ROMERO-GARCÍA V., PICÓ R., CEBRECOS A. *et al.*, "Enhancement of sound in chirped sonic crystals", *Applied Physics Letters*, vol. 102, no. 9, p. 091906, 2013.

[ROM 16a] ROMERO-GARCÍA V., THEOCHARIS G., RICHOUX O. *et al.*, "Perfect and broadband acoustic absorption by critically coupled sub-wavelength resonators", *Scientific Reports*, vol. 6, p. 19519, 2016.

[ROM 16b] ROMERO-GARCÍA V., THEOCHARIS G., RICHOUX O. *et al.*, "Use of complex frequency plane to design broadband and sub-wavelength absorbers", *Journal of the Acoustical Society of America*, vol. 139, no. 6, p. 3395, 2016.

[SCH 75] SCHRÖDER M.R., "Diffuse sound reflection by maximum- length sequences", *Journal of the Acoustical Society of America*, vol. 57, no. 1, pp. 149–150, 1975.

[STI 91] STINSON M.R., "The propagation of plane sound waves in narrow and wide circular tubes, and generalization to uniform tubes of arbitrary cross-sectional shape", *Journal of the Acoustical Society of America*, vol. 89, no. 2, pp. 550–558, 1991.

[THE 14] THEOCHARIS G., RICHOUX O., ROMERO-GARCÍA V. *et al.*, "Limits of slow sound propagation and transparency in lossy, locally resonant periodic structures", *New Journal of Physics*, vol. 16, no. 9, p. 093017, 2014.

[TSA 07] TSAKMAKIDIS K.L., BOARDMAN A.D., HESS O., "Trapped rainbow storage of light in metamaterials", *Nature*, vol. 450, no. 7168, pp. 397–401, 2007.

[YAN 08] YANG Z., MEI J., YANG M. *et al.*, "Membrane-type acoustic metamaterial with negative dynamic mass", *Physical Review Letters*, vol. 101, no. 20, p. 204301, 2008.

[YAN 15] YANG M., MENG C., FU C. *et al.*, "Subwavelength total acoustic absorption with degenerate resonators", *Physical Review Letters*, vol. 107, no. 10, p. 104104, 2015.

[ZHU 13] ZHU J., CHEN Y., ZHU X. *et al.*, "Acoustic rainbow trapping", *Scientific Reports*, vol. 3, 2013.